AGU PUBLICATIONS

JGR

Journal of Geophysical Research: Space Physics

RESEARCH ARTICLE
10.1002/2016JA023217

Key Points:
- The first model of the inner/near magnetosphere with no a priori assumptions on the field source geometry
- Input drivers include interplanetary and ground observables (Pdyn, *SYM-H*, Newell's *N*-index, and IMF B_y)
- Based on the largest ever amount of data and yields the highest ever merit parameters/correlations

Correspondence to:
N. A. Tsyganenko,
n.tsyganenko@spbu.ru

Citation:
Tsyganenko, N. A., and V. A. Andreeva (2016), An empirical RBF model of the magnetosphere parameterized by interplanetary and ground-based drivers, *J. Geophys. Res. Space Physics*, *121*, 10,786–10,802, doi:10.1002/2016JA023217.

Received 21 JUL 2016
Accepted 17 OCT 2016
Accepted article online 24 OCT 2016
Published online 5 NOV 2016

An empirical RBF model of the magnetosphere parameterized by interplanetary and ground-based drivers

N. A. Tsyganenko[1] and V. A. Andreeva[1]

[1] Institute and Department of Physics, Saint Petersburg State University, Saint Petersburg, Russia

Abstract In our recent paper (Andreeva and Tsyganenko, 2016), a novel method was proposed to model the magnetosphere directly from spacecraft data, with no a priori knowledge nor ad hoc assumptions about the geometry of the magnetic field sources. The idea was to split the field into the toroidal and poloidal parts and then expand each part into a weighted sum of radial basis functions (RBF). In the present work we take the next step forward by having developed a full-fledged model of the near magnetosphere, based on a multiyear set of space magnetometer data (1995–2015) and driven by ground-based and interplanetary input parameters. The model consolidates the largest ever amount of data and has been found to provide the best ever merit parameters, in terms of both the overall RMS residual field and record-high correlation coefficients between the observed and model field components. By experimenting with different combinations of input parameters and their time-averaging intervals, we found the best so far results to be given by the ram pressure P_d, *SYM-H*, and *N*-index by Newell et al. (2007). In addition, the IMF B_y has also been included as a model driver, with a goal to more accurately represent the IMF penetration effects. The model faithfully reproduces both externally and internally induced variations in the global distribution of the geomagnetic field and electric currents. Stronger solar wind driving results in a deepening of the equatorial field depression and a dramatic increase of its dawn-dusk asymmetry. The Earth's dipole tilt causes a consistent deformation of the magnetotail current sheet and a significant north-south asymmetry of the polar cusp depressions on the dayside. Next steps to further develop the new approach are also discussed.

1. Introduction

In our previous publication [*Andreeva and Tsyganenko*, 2016, hereinafter AT16], a new approach was described to quantitatively model the magnetospheric magnetic field with no a priori assumptions on the geometry of associated electric currents. In essence, it is a synthesis of two methods, of which the first one is to represent the field as a sum of toroidal and poloidal parts [e.g., *Elsasser*, 1946; *Wolf-Gladrow*, 1987] and the latter one is to expand each of the corresponding generating potentials into a sum of radial basis functions (RBF) [e.g., *Buhmann*, 2003]. As demonstrated in AT16, the idea to combine these two approaches offers a viable and much more flexible alternative to the standard empirical models based on the modular principle [e.g., *Tsyganenko*, 2013]. The new method was found to be able to resolve even fine details of the observed magnetic field structure, hardly detectable by the traditional models.

In the first experiments described in AT16, we fitted the model field to only four relatively small data subsamples, each containing on the order of ~40,000 records and representing four typical states of the magnetosphere before and during a disturbance. The natural next step forward is then to extend the proposed technique to a full-fledged model driven by routinely available interplanetary/ground observables and calibrated against the entire "grand" set of spacecraft data. This paper presents first results of such an effort and discusses future applications of the new approach.

The paper consists of seven sections. Section 2 concisely recapitulates the essence of the RBF model presented earlier in AT16. Section 3 briefly describes the data sets and missions they came from. Section 4 addresses the issue of the model parameterization. Section 5 presents main results of fitting the model to data in the form of model/data scatterplots and illustrates them with plots of equatorial and meridional field/current distributions. In section 6 we show first results of validating the model using independent geosynchronous data, discuss limitations of the present version, and outline the most important issues to concentrate on in future studies. Section 7 summarizes the paper.

2. RBF Model Formulation

The essence of the method is to represent the external field, with the Earth's contribution subtracted, as the sum of its toroidal and poloidal parts [see, e.g., *Stern*, 1976]:

$$\mathbf{B}(\mathbf{r}) = \nabla \times (\Psi_1 \mathbf{r}) + \nabla \times \nabla \times (\Psi_2 \mathbf{r}) = \nabla\Psi_1 \times \mathbf{r} + \nabla \times (\nabla\Psi_2 \times \mathbf{r}) \tag{1}$$

and then to expand the corresponding generating functions $\Psi_1(\mathbf{r})$ and $\Psi_2(\mathbf{r})$ into linear combinations of radial basis functions having the form

$$\Psi_{1,2}(\mathbf{r}) = \sum_{i=1}^{N} a_{i_{1,2}} \chi_i(\mathbf{r}) \text{ , where } \chi_i(\mathbf{r}) = \sqrt{|\mathbf{r} - \mathbf{R_i}|^2 + D^2} \tag{2}$$

The nodes $\mathbf{R}_i$ of the RBF meshwork are distributed within the modeling domain at N prescribed fixed locations on both sides of the solar-magnetic (SM) equatorial plane, and each basis function in the sums includes a regularization term D^2. The coefficients $a_{i_{1,2}}$ are free model parameters quantifying contributions to the total field from individual RBF nodes, calculated by fitting the model (1) to an experimental set of spacecraft magnetometer data. A remarkable advantage of this approach is its flexibility, achieved by placing a sufficiently large number of nodes over the modeling domain. Another benefit of the method is the possibility to locally adjust the density of RBF centers to improve the fit quality in specific regions.

In order to take into account the magnetospheric symmetry properties and the dipole tilt effects, the approach adopted in AT16 was to first compose partial RBFs χ_i^+ and χ_i^-, even and odd with respect to Z_{SM} coordinate, and then write down the desired generating functions as

$$\Psi_1 = \cos\psi \sum_{i=1}^{N} a_i \left(\chi_i^+ + \chi_i^-\right) + \sin\psi \sum_{i=1}^{N} b_i \left(\chi_i^+ - \chi_i^-\right) \tag{3}$$

$$\Psi_2 = \cos\psi \sum_{i=1}^{N} c_i \left(\chi_i^+ - \chi_i^-\right) + \sin\psi \sum_{i=1}^{N} d_i \left(\chi_i^+ + \chi_i^-\right) \tag{4}$$

where ψ is the dipole tilt angle and a_i, b_i, c_i, and d_i are unknown model coefficients. Thus defined toroidal Ψ_1 and poloidal Ψ_2 potentials ensure that the resulting field components have the required parity, such that the model configurations are mirror-symmetric with respect to the simultaneous change of sign $\{z \to -z,\ \psi \to -\psi\}$ (see AT16, equation (4)). Explicit equations for the magnetic field components derived from (3) and (4) were given in the AT16 supporting information, and the reader is referred to that source for more details.

In the present realization of the model, one more component has been added on top of the field of principal magnetospheric sources given by (3) and (4). Namely, we introduced a term representing the IMF B_y "penetration" inside the magnetosphere, an effect most prominently observed inside the high plasma beta regions such as the tail plasma sheet [e.g., *Sergeev*, 1987; *Lui*, 1986; *Kaymaz et al.*, 1994] and in the polar cusps [*Tsyganenko*, 2009]. In both cases, the physical interpretation of the penetration effect is closely related to the field-aligned currents flowing on the boundaries of those regions.

The symmetry properties of the penetrated IMF B_y are different from those of the principal field. First of all, we assume that the penetrated B_y, to the lowest approximation, does not depend on the dipole tilt. On the premises that (1) the externally imposed IMF is strictly azimuthal and (2) the magnetopause is axisymmetric, we also conclude that the penetrated field must obey the same symmetry relations as the external field (which can be illustrated by simple magnetostatic problems). Specifically, both $B_x^{(p)}$ and $B_y^{(p)}$ components of the penetrated field must be even and $B_z^{(p)}$ component must be odd with respect to z. Based on this condition and equations for Cartesian components of the toroidal and poloidal fields (equations (2)–(6) in the AT16 supporting information), one can easily infer that the toroidal $\Psi_1^{(p)}$ and poloidal $\Psi_2^{(p)}$ generating functions of the penetrated field must be, respectively, even and odd with respect to z.

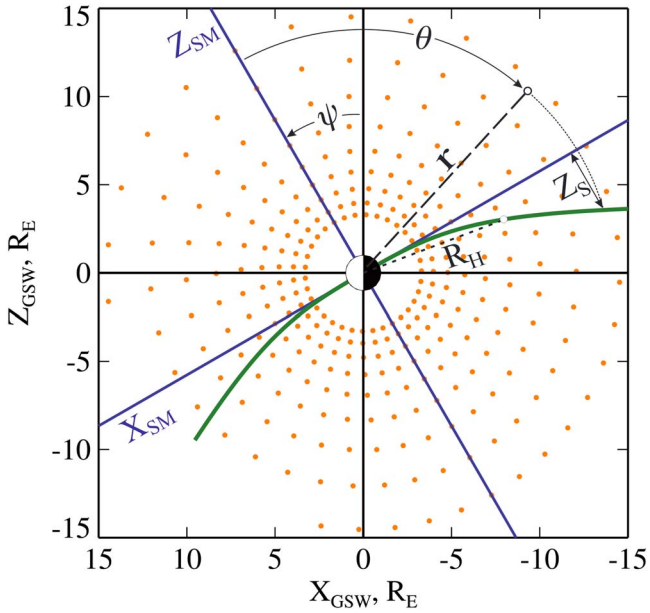

Figure 1. Illustrating the tilt-induced deformation of the RBF grid as quantified by equations (7) and (8). The green line is the intersection of the bowl-shaped equatorial sheet defined by equation (7), and the orange dots show the RBF meshwork nodes located in the noon-midnight meridian plane.

In view of the above, the generating potentials for the toroidal $\Psi_1^{(p)}$ and poloidal $\Psi_2^{(p)}$ parts of the penetrated field (hence the superscript "p") take the form

$$\Psi_1^{(p)} = \sum_{i=1}^{N} e_i \left(\chi_i^+ - \chi_i^- \right) \tag{5}$$

$$\Psi_2^{(p)} = \sum_{i=1}^{N} f_i \left(\chi_i^+ + \chi_i^- \right) \tag{6}$$

with e_i and f_i being the corresponding unknown free coefficients. As shown below in section 5, adding the effect of penetrated IMF B_y significantly improves the correlation between the observed and modeled y components of the magnetospheric field and removes artifacts that persistently stuck out in all earlier models.

The RBF node meshwork was generated using essentially the same method by *Kurihara* [1965] as described in AT16 but with an additional modification of the grid in the case $\psi \neq 0$. More specifically, when test-fitting the model to artificially generated "data" sets, a tangible improvement was found to arise from applying a radially dependent rotation of the nodes, consistent with the tilt-related bending/warping of the equatorial current sheet [e.g., *Tsyganenko and Andreeva*, 2014, hereinafter TA14]. In more detail, each RBF node located at a geocentric distance r and solar-magnetic (SM) colatitude θ gets an additional shift in the polar angle (see Figure 1):

$$\Delta\theta(r,\theta) = -\sin(\theta) \arcsin \frac{Z_S(r,\psi)}{r} \tag{7}$$

where $Z_S(r,\psi)$ is the deviation of the bowl-shaped current surface from the SM equatorial plane:

$$Z_S(r,\psi) = R_H \tan\psi \left\{ 1 - \left[1 + \left(\frac{r}{R_H} \right)^{\alpha} \right]^{1/\alpha} \right\} \tag{8}$$

similar to equation (1) of TA14 but with ρ now replaced by the radial distance r. The parameter R_H is the hinging distance, and the exponent α controls the smoothness of the sheet bending at the distance $r \sim R_H$ where it departs from the SM equatorial plane. Equations (7) and (8) ensure that at small $r \ll R_H$ the RBF grid is almost

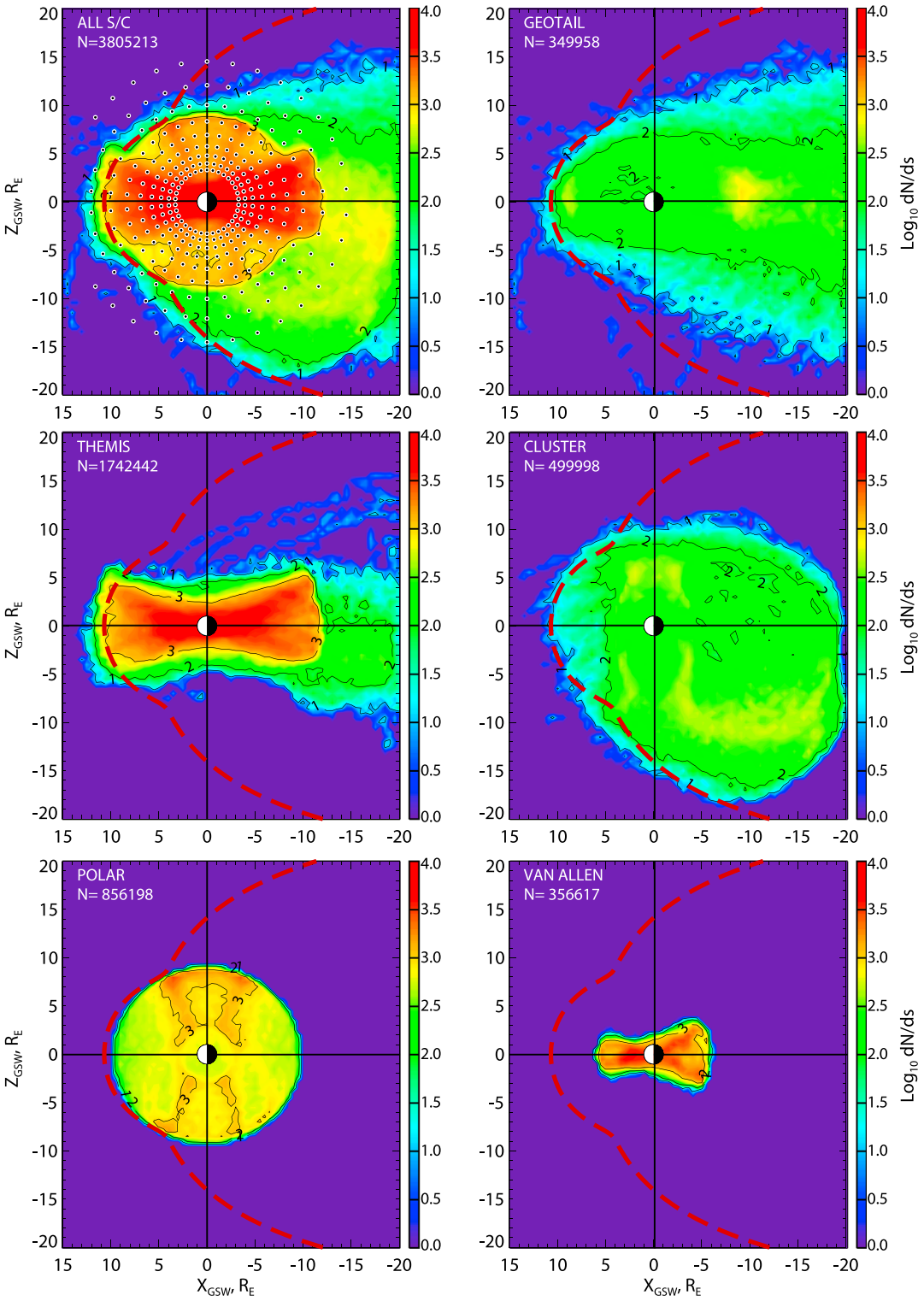

Figure 2. Illustrating the data coverage in projection on the geocentric solar-wind (GSW) meridian plane. The six panels display the data density in the entire modeling set and for each individual mission. Top left panel also shows the distribution of the RBF nodes lying in the meridional plane $Y_{GSW} = 0$.

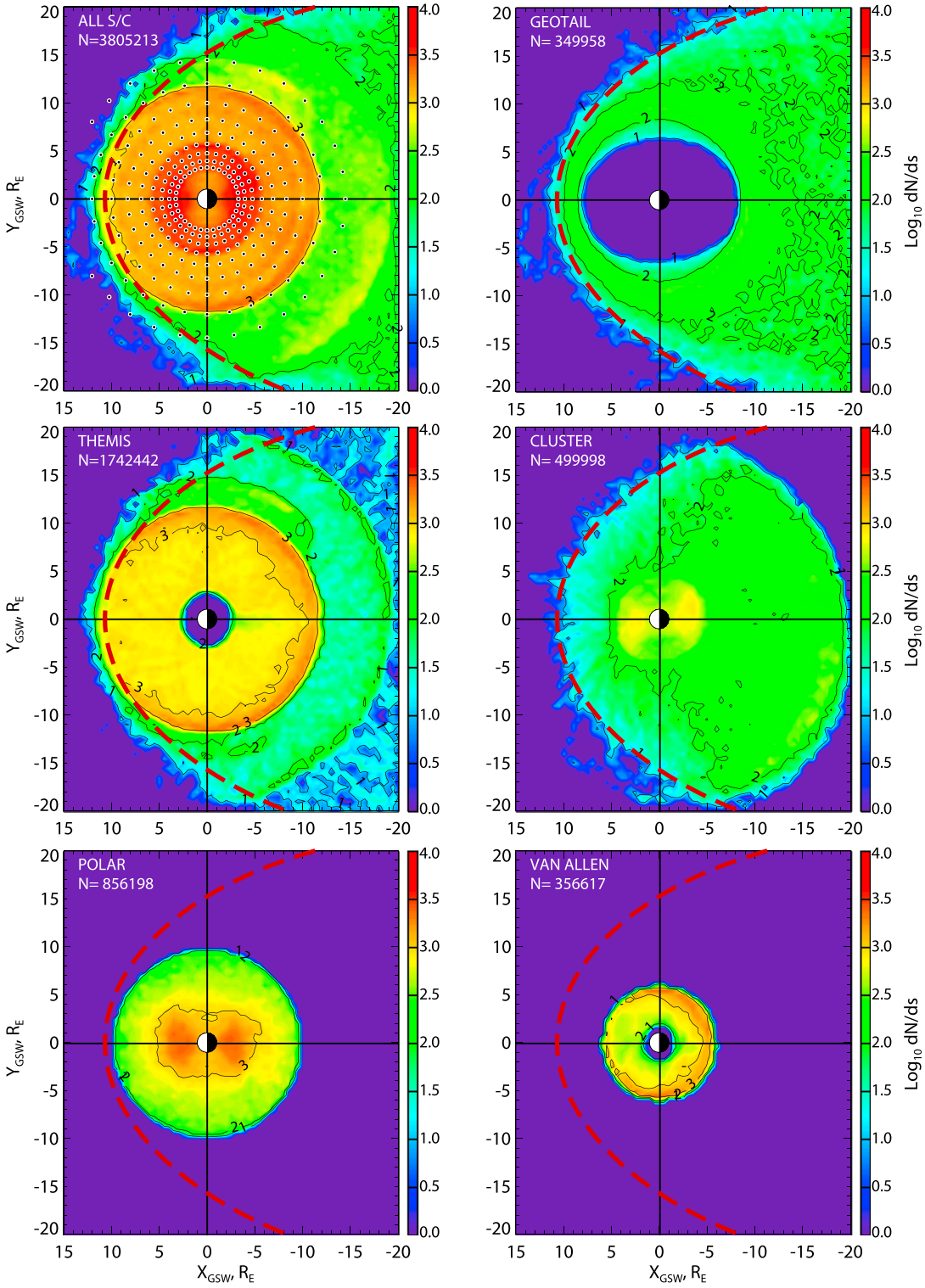

Figure 3. Same as in Figure 2 but in projection on the equatorial plane $Z_{GSW} = 0$.

rigidly controlled by the geodipole orientation (i.e., remains nearly fixed in the SM coordinates) but gradually slips behind with growing $r \geq R_H$ and becomes virtually uncoupled from the dipole rotation at $r \gg R_H$ in the tail. The $\sin\theta$ factor in (7) is added to introduce a gradual decrease of the deformation magnitude from its maximum value at the SM equator to zero at the Z_{SM} axis.

In the present version of the model we used a meshwork consisting of $N = 1296$ RBF nodes (per each hemispace, above and below the SM equator) distributed over nine concentric spheres, with the innermost and the outermost radii being $R_1 = 3.3\,R_E$ and $R_9 = 14.5\,R_E$, respectively. Each spherical surface holds 144 nearly equidistant nodes per hemisphere, so that the average distance between neighboring nodes ranges between $\sim 0.7\,R_E$ at $r = R_1$ and $\sim 3\,R_E$ at $r = R_9$. The deformation parameters in (8) were set at $R_H = 8\,R_E$ and $\alpha = 3$, corresponding to their average estimates obtained in our earlier studies of the tilt-related effects [e.g., *Tsyganenko and Fairfield*, 2004; *Tsyganenko and Andreeva*, 2015, hereinafter TA15]. The radial, latitudinal, and longitudinal distributions of the RBF nodes in the untilted case $\psi = 0$ are also illustrated below in the top left panels of Figures 2 and 3.

3. Data

The "grand" set of spacecraft magnetometer data used in this work is essentially the same collection of 5 min average field vectors as that described in our earlier studies [*Tsyganenko et al.*, 2015; AT16; TA15]. Those publications gave a fairly detailed account of the database, source missions, and procedures involved in its creation. In order to save page space and avoid long repetitive descriptions migrating from one paper to another, we restrict this section to a concise synopsis of relevant general information with a list of the most recent upgrades and provide a set of plots illustrating the data spatial and temporal coverage.

Overall, the entire grand database covers the period from 1995 to 2015 and the range of geocentric distances between 2 and $\sim 150\,R_E$ within the magnetosphere. The total number of 5 min average magnetic field vectors in the set equals 4,140,712, which includes the data by Geotail, Polar, Cluster, Time History of Events and Macroscale Interactions during Substorms (THEMIS)/Acceleration, Reconnection, Turbulence and Electrodynamics of Moon's Interaction with the Sun (ARTEMIS), and Van Allen (Radiation Belt Space Probes (RBSP)). We discarded from the outset the deep tail data by narrowing down the distance interval to $2 \leq r \leq 60\,R_E$, which slightly reduced the number of records to 4,109,178. In this particular study, the modeling region was further limited to the inner and high-latitude magnetosphere by setting the tailward boundary of data selection region at $X_{GSW} = -20\,R_E$, which brought the number of records in the subset down to 3,805,213. Here we note in passing that both position and magnetic field vectors are represented in the aberrated geocentric solar-wind (GSW) coordinate system with the x axis antiparallel to the current solar wind direction [e.g., *Hones et al.*, 1986; *Tsyganenko et al.*, 1998, 2015]. Unlike in the previous modeling projects (e.g., in the TA15 model), no restrictions were imposed on the interplanetary parameters nor on the ground-based *SYM-H* index.

In the most recent version of the database, each record is tagged with not only the concurrent solar wind/IMF parameters but also with sliding masked averages of the corrected *SYM-H* index, $\langle SYMH_c \rangle$, and its time derivative $\langle DSYMH_c/Dt \rangle$, the *N*- and *B*-indices by *Newell et al.* [2007] and *Boynton et al.* [2011], and, finally, the polar cap PC-index [e.g., *Troshichev and Janzhura*, 2012]. Among the goals of this study was to seek for an optimal combination of input parameters providing the minimal deviation of the model field from data, which motivated us to include all the various indices within each single data record in the set. More details on the external parameter computation, averaging, etc., will be given below in section 4.

Figures 2 and 3 illustrate the spatial coverage by the data of the modeling region in the meridional (Figure 2) and equatorial (Figure 3) projections. The color-coded quantity is the logarithm of the number of data points falling, respectively, within $\Delta X \times \Delta Z$ and $\Delta X \times \Delta Y$ columns with $\Delta X = \Delta Y = \Delta Z = 0.5\,R_E$. Top left panels in both figures show cumulative distributions of data from all missions taken together and the locations of the meridional (Figure 2) and near-equatorial (Figure 3) RBF nodes. The other five panels in each of the two figures illustrate partial contributions from individual missions, as labeled on the diagrams. In general, the data point density is largely nonuniform, with the highest coverage in the inner low-latitude magnetosphere, mostly owing to the data by THEMIS, Polar, and Van Allen probes. The data density is much lower in the tail lobes and in the distant plasma sheet; nevertheless, due to the long time span of the Geotail and Cluster missions, the coverage is fairly continuous, without outstanding gaps. In the previous empirical models based on the modular principle, the spatial nonuniformity of data was justly considered as an adverse factor, and

special measures were taken to equalize the weights of observations taken in regions with largely different data density [e.g., *Tsyganenko and Sitnov*, 2007, section 5.2]. In the present approach there is no need in such a weighting, and the evenness of the data coverage is of secondary importance. Indeed, by the very nature of our method based on a relatively dense meshwork of the RBF centers, contributions from individual nodes become uncoupled on the large scale, so that the fitting procedure flexibly consolidates the nonuniformly distributed data into a single model.

At the same time, one should nevertheless keep in mind the nonuniformity of data in the parametric space: a steep growth in the data density toward the low end of the disturbance scale and, conversely, its dramatic decline with increasing geomagnetic activity. That problem was discussed at length in section 3 of TA15, and a special thinning algorithm was developed in that work to minimize the data disparity. The essence of the procedure was to define a threshold value N_c of the normalized interplanetary N-index [*Newell et al.*, 2007; TA15]:

$$N = 10^{-4} V^{4/3} B_{\perp}^{2/3} \sin^{8/3} \frac{\theta_c}{2} \tag{9}$$

(V and $B_{\perp}$ in km/s and nT, respectively), such that all data records with $N \geq N_c$ were unconditionally retained in the output subset, while those with $N < N_c$ were either rejected or retained depending on whether or not a randomly generated number from the interval [0, 1] fell below $10^{1.36(N-N_c)}$. The rule was based on the obtained rate of the exponential falloff of the data density as a function of the N-index (see TA15, Figure 2). In the present work, we adopted that method without any modifications and with the same threshold value $N_c = 1$, which resulted in a further fivefold reduction of the data subsample size down to 732,746 records. Just for the reader's orientation, the threshold $N_c = 1$ nearly coincides with the 95% containment boundary of the data distribution. For the solar wind speed of 400 km/s, that value corresponds to a purely southward IMF $B_z \approx -6$ nT (see TA15, Figures 1 and 2, for more details).

4. Parameterization

The essence of the parameterization is to define a functional relationship between the linear and nonlinear parameters of a model and its external input expressed in terms of ground activity indices and/or interplanetary drivers. In the case of a modular model with a relatively small number of parameters, it is possible to seek the magnitudes of individual current systems (modules) as solutions of dynamical equations representing their variation as a result of competition between the external driving and internal losses. In that formulation, the relaxation and response time scales are treated as unknown nonlinear parameters to be found from data. That approach was at the core of the TS05 model [*Tsyganenko and Sitnov*, 2005], specially designed to reproduce the storm time dynamics of the inner magnetosphere. In the framework of the present model, the RBF nodes can also be formally viewed as individual field sources, and each of them can in principle be parameterized by means of dynamical driving relaxation equations similar to those used in TS05. However, since the relaxation time scales are essentially nonlinear parameters and in view of the very large number of the RBF nodes, such an approach is out of the question as being infeasible from the computation viewpoint. Another completely different parameterization method based on a data-mining technique was employed in the TS07D model [*Tsyganenko and Sitnov*, 2007; *Sitnov et al.*, 2008, 2010; *Stephens et al.*, 2013, 2016]. That method appears as a more realistic alternative, and we plan to explore it in a separate future study.

In the present work, we restricted ourselves to a simpler parameterization scheme, which is to expand each RBF node magnitude coefficient into a linear combination of standard, readily available interplanetary and ground-based parameters, representing a few basic modes of response with largely different time scales. The first and the most influential external driver is the solar wind dynamic pressure P_d, whose variations rapidly impact the entire magnetosphere. The second independent parameter quantifying the state of the inner equatorial domain is the corrected *SYM-H* index: $SYM\text{-}H_c = 0.8 \cdot SYM\text{-}H - 13\sqrt{P_d}$ [e.g., *Tsyganenko*, 1996], which highly correlates with the intensity of the symmetric and partial ring current and has a relatively slow response and relaxation time scale (up to many hours). A third parameter is needed to represent faster and more dynamic high-latitude field sources, such as the cusp diamagnetic and Region 1 field-aligned currents, most directly exposed to the magnetosheath and solar wind plasma flow. At an early stage of this work, we experimented with a few variables as appropriate candidate quantifiers of the direct interplanetary driving. In particular, sliding averages of the $SYM\text{-}H_c$ time derivative $D\langle SymH_c\rangle/Dt$ were tested, first introduced in

Sitnov et al. [2008] and defined by equation (10) of AT16, as well as the polar cap PC-index [e.g., *Troshichev and Janzhura*, 2012]. Although adding each of those parameters at a time improved the model's performance, the best results were obtained with the *N*-index (9), slide averaged over preceding half-hour intervals. The presence in the RBF expansions of two indices, *SYM-H*$_c$ and *N*, with largely different response time scales is intended to ensure a proper representation of contributions from the convection-energization processes in the inner magnetosphere, on the one hand, and much faster energy/mass injection effects at higher L shells on the other.

Finally, to include the above discussed effect of the azimuthal IMF penetration, the corresponding RBF expansions (5) and (6) were factored with the IMF B_y. In summary, the model coefficients in the expansions (3)–(6) for the toroidal and poloidal generating potentials were assumed in the form

$$a_i = a_{i0} + a_{i1}\left(\sqrt{\frac{P_d}{P_{d0}}} - 1\right) + a_{i2}\frac{\langle SYM\text{-}H_c\rangle}{50} + a_{i3}\langle N\rangle \tag{10}$$

$$b_i = b_{i0} + b_{i1}\left(\sqrt{\frac{P_d}{P_{d0}}} - 1\right) + b_{i2}\frac{\langle SYM\text{-}H_c\rangle}{50} + b_{i3}\langle N\rangle \tag{11}$$

$$c_i = c_{i0} + c_{i1}\left(\sqrt{\frac{P_d}{P_{d0}}} - 1\right) + c_{i2}\frac{\langle SYM\text{-}H_c\rangle}{50} + c_{i3}\langle N\rangle \tag{12}$$

$$d_i = d_{i0} + d_{i1}\left(\sqrt{\frac{P_d}{P_{d0}}} - 1\right) + d_{i2}\frac{\langle SYM\text{-}H_c\rangle}{50} + d_{i3}\langle N\rangle \tag{13}$$

and

$$e_i = e_{i0}\frac{\langle B_y^{(\mathrm{IMF})}\rangle}{B_{y0}} \qquad f_i = f_{i0}\frac{\langle B_y^{(\mathrm{IMF})}\rangle}{B_{y0}} \tag{14}$$

where $P_{d0} = 2$ nPa and $B_{y0} = 5$ nT. The corrected *SYM-H*$_c$ enters in (10)–(13) in the form of centered sliding masked averages $\langle SYM\text{-}H_c\rangle$ calculated over ±15 min intervals, while $\langle N\rangle$ and $\langle B_y^{(\mathrm{IMF})}\rangle$ were slide averaged over preceding half-hour intervals.

5. Results

As detailed above, the model field expansions (3)–(6) are composed of 1296 north-south symmetric pairs of the basis functions, $(\chi_i^+ + \chi_i^-)$, and of the same number of antisymmetric pairs, $(\chi_i^+ - \chi_i^-)$, each pair multiplied by nine coefficients entering in (10)–(14): $\{a_{ik}, d_{ik}, f_i\}$ and $\{b_{ik}, c_{ik}, e_i\}$, respectively ($i = 1, \ldots, 1296$, $k = 0, 1, 2, 3$). In total, this yields 23,328 unknown coefficients to be calculated as the solution of a system of 23,328 linear normal equations, minimizing the RMS difference between the observed and model field vectors over the entire set of 732,746 data records. The derivation of the model coefficients was carried out in two steps by separate codes, of which the first one calculated the elements of the left-hand side matrix and the right-hand side vector. Because of the large size of the data set, the involved summation procedure was parallelized and the resulting output files were stored on disk. At the second step, the files were read back into the memory, the matrix was inverted using a singular value decomposition (SVD) algorithm [*Press et al.*, 1992], and the desired solution was finally obtained in the form of a set of model coefficients. An important aspect of the SVD method is a somewhat subjective choice of the tolerance parameter that prescribes a lower limit on the matrix singular values and thus defines its condition number [e.g., *Gershenfeld*, 2003, chapter 10.3]. In our numerical experiments it was found that setting the ratio of the smallest to the largest singular value at 10^{-10} provided an apparently optimal tradeoff between the model's resolution and the magnitude of artificial "bumps" in the model field distribution.

We quantify the overall fidelity of the fitted model field $\mathbf{B}_{\mathrm{mod}}$ by the figure of merit expressed in terms of the ratio of the RMS residual field $Q = \langle(\mathbf{B}_{\mathrm{obs}} - \mathbf{B}_{\mathrm{mod}})^2\rangle^{1/2}$ to the RMS observed external field $\langle\mathbf{B}_{\mathrm{obs}}^2\rangle^{1/2}$. The above described version of the RBF model yielded $Q = 13.42$ nT, which is only 34% of $\langle\mathbf{B}_{\mathrm{obs}}^2\rangle^{1/2} = 39.38$ nT, the best

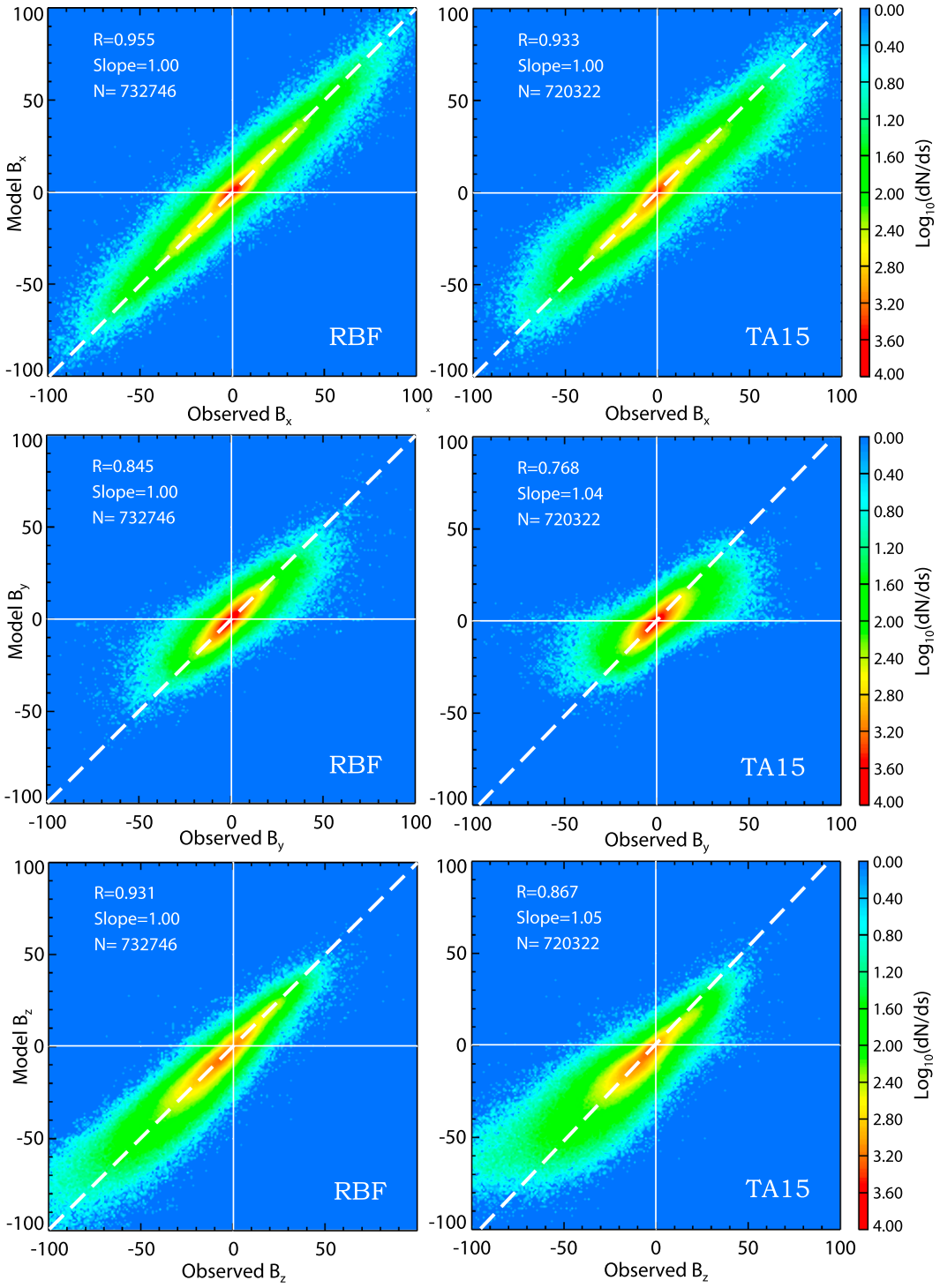

Figure 4. Scatterplots of the model versus observed magnetic field GSW components. (left column) RBF B_x (top), B_y (middle), and B_z (bottom). (right column) The same but for the TA15 model. The color quantifies the data density distribution on the logarithmic scale (see text for details).

figure of merit ever obtained in the empirical modeling. For comparison, in the T02 model [*Tsyganenko*, 2002a, 2002b] based on a sixteenfold smaller data set (45,202 data records) with nearly the same spatial extent of the modeling domain, the figure of merit was 42.4%. Testing the recent modular TA15 model against a subsample of the present data set with 720,323 records gave the figure of merit ~43% (due to a limited allowable range of TA15 input parameters, in the latter case we had to slightly reduce the data set by having excluded 1.7% of data records with $N > 2$).

The most convincing illustration of the superiority of the RBF model over the earlier ones based on the modular approach is presented in Figure 4. Figure 4 (left column) shows three scatterplots of GSW components of the observed against the RBF model field. Figure 4 (right column) displays the corresponding result for the TA15 model (as already noted above, obtained on a slightly smaller data set). The plots are analogous to Figure 15 of TA15, except how the data are presented: (a) the axes orientation is swapped, so that the model/observed **B** components are now plotted along the horizontal/vertical axes, and (b) a more informative method is employed to visualize the data scatter around the diagonal. Namely, instead of directly plotting a monochrome blot-like cloud of dots each representing an individual data record, we divide the plotting area into square bins 1 nT × 1 nT and color them according to the number of data points falling in each bin, on a logarithmic scale.

The resulting distributions reveal a bright red/yellow central core, stretched along the diagonal and containing most part of the data, enveloped within a much sparser green/blue "penumbra," with the following notable details. First, the penumbras in all the panels are slightly tilted clockwise with respect to the main diagonal, revealing a somewhat underdeformed model field for strongly disturbed periods. Nevertheless, the best fit slopes for all three components are equal to unity, due to the overwhelming dominance of the inner core data. Second, in spite of the very large number of records in the fitting data set, the correlation coefficients between the observed and the model field components ({0.955, 0.845, 0.931} for $\{B_x, B_y, B_z\}$, respectively) are record-high when compared to those obtained earlier in the previous models. Thus, the corresponding correlation coefficients for the T96, T02, and TA15 models had been found equal to {0.89, 0.65, 0.81}, {0.92, 0.67, 0.87}, and {0.93, 0.77, 0.87}, respectively. Third, as can be seen from these values, the most dramatic improvement has been achieved for the B_y component. This is evident from comparing the corresponding plots in Figure 4 (middle row): the TA15 distribution (right) has a significantly lower correlation and a stronger asymmetry of the penumbral data with respect to the diagonal. That feature was found to be even more pronounced in the older T96 and T02 models, where the B_y scatterplots included an extended and narrow streak which revealed the inability of those models to replicate the effect of Region 0 field-aligned currents induced on the dayside by the azimuthal component of the IMF [*Tsyganenko*, 2009] (see, e.g., Figures 9 and 10 in T02).

To illustrate the model's performance in replicating the global magnetospheric structure for different disturbance levels, we plotted in Figure 5 the meridional (left column) and equatorial (right column) distributions of the field compression and depression, expressed in terms of the scalar difference $\Delta B = |\mathbf{B}_{\text{total}}| - |\mathbf{B}_{\text{dipole}}|$. Figure 5 (top and bottom rows) correspond to very quiet (vq) and strongly disturbed (sd) conditions, which we somewhat arbitrarily specified by setting the following values of the solar wind pressure P_d, *SYM-H*, and *N*-index: $\{1.5, 0, 0\}$ (vq) and $\{4, -150, 2\}$ (sd). We specially note here that the bounding contour confining the colored areas in all the panels does not have anything to do with the present field model: it rather corresponds to the magnetopause by *Lin et al.* [2010], plotted in the figures only for the reader's orientation, in order to better visualize the location of the model field structures (e.g., the cusps) with respect to the anticipated boundary position.

As expected, larger values of the above control parameters result in progressively stronger tail lobe field and deeper field depressions in the inner equatorial magnetosphere and in the outer cusps. In Figure 5 (right column), a roughly dawn-dusk symmetric quiet configuration (top) evolves into a severely asymmetric storm time distribution (bottom), in which the field depression closely approaches and tightly envelops the Earth, with the duskside field lower by 100–150 nT than at dawn. Unlike in the earlier modular models, the equal ΔB contours are not perfectly smooth and have some wiggles, which is a natural consequence of the discrete nature of the RBF meshwork in combination with the inevitable nonuniformity of the data coverage. Nevertheless, the overall ΔB distribution is reasonably regular, in particular, around the tail current sheet on the nightside, confirming the feasibility of the approach to replicate the average magnetospheric

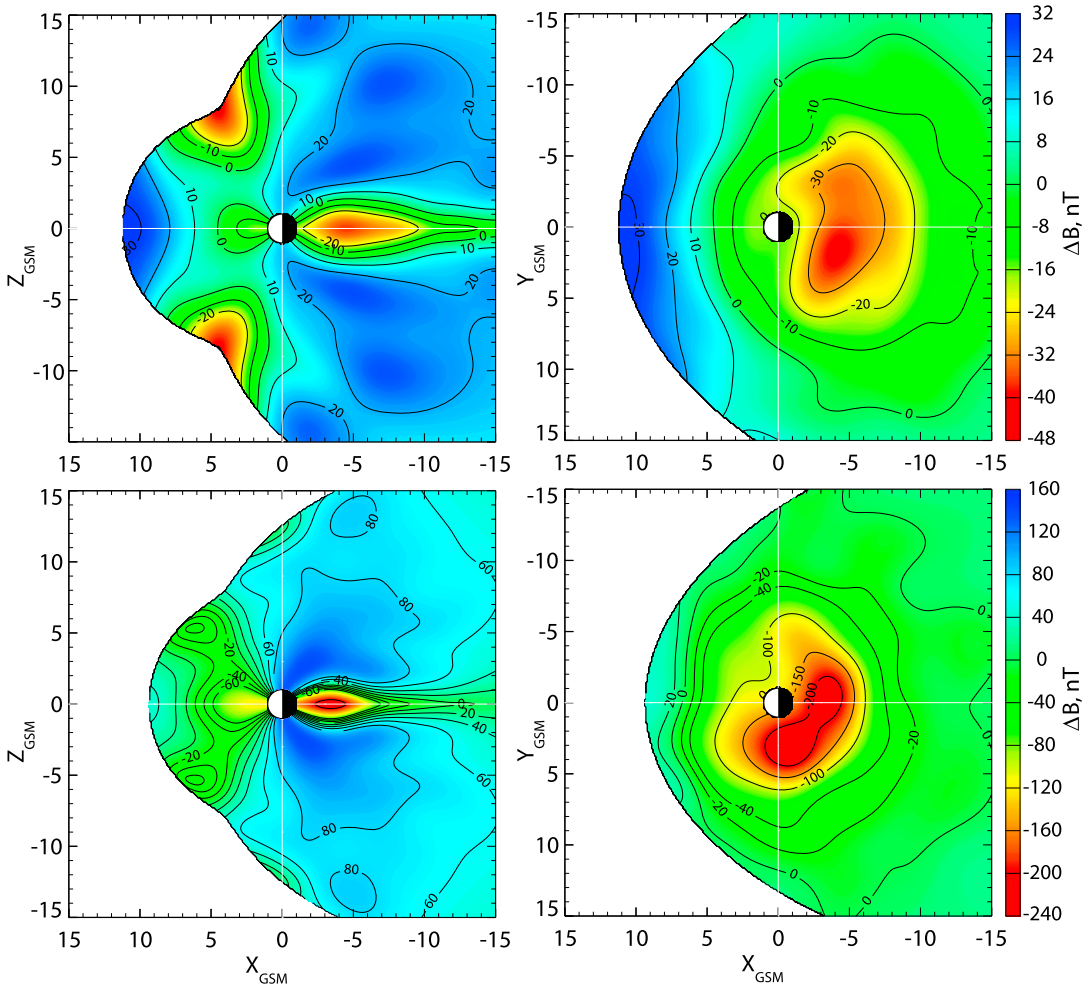

Figure 5. (left column) Meridional and (right column) equatorial distributions of $\Delta B = |\mathbf{B}_{\text{total}}| - |\mathbf{B}_{\text{dipole}}|$ for two sets of the model parameters, corresponding to (top row) very quiet and (bottom row) strongly disturbed conditions, as specified in the text. Note the fivefold difference in the color scale range. The *Lin et al.* [2010] magnetopause contour bounding the modeling region is not a part of the present model and has been added only for the reader's orientation.

structure. It is also worth noting that in both examples the low-altitude longitude-averaged equatorial depression consistently matches the input values of *SYM-H*.

In the above test examples, all three input parameters, P_d, *SYM-H*, and *N* were set to grow from low to high values. While it is of certain interest to explore in detail how the model responds to separate variations of each of its input parameters, that question extends beyond the scope and page limits of this work and will be addressed in a separate publication.

We complete this section with a brief examination of the dipole tilt angle effects in the RBF model. Figure 6 displays two meridional plots of the model ΔB in the same format as in Figure 5, but for the maximum value of the tilt angle $\psi = 30°$ and two values of the *N*-index, $N = 0$ (left) and $N = 2$ (right), corresponding to two extreme situations in terms of the interplanetary magnetic flux intake rate. In both cases, the solar wind pressure and *SYM-H* index were assumed equal to 2 nPa and 0 nT, respectively. The most outstanding effects clearly seen on the dayside are (a) a dramatic asymmetry between the northern and southern cusp depressions and (b) much deeper penetration of the depressed field regions in the case of strong interplanetary driving, taking place in both hemispheres. On the nightside, large *N* results in much deeper equatorial depression and stronger lobe fields. One can also see the well-studied tilt-related effect of bending/hinging of the equatorial current [e.g., *Tsyganenko et al.*, 2015 and references therein], manifested here in a similar deformation of the ΔB isointensity contours. It is interesting to note that even a more subtle effect shows up on the nightside, namely, the difference in the shapes of the outer equatorial sheet in the $N = 0$ and $N = 2$ cases. While in the former case the bending saturates at $X \leq -10$, in the latter case the sheet continues to depart from the GSM equator,

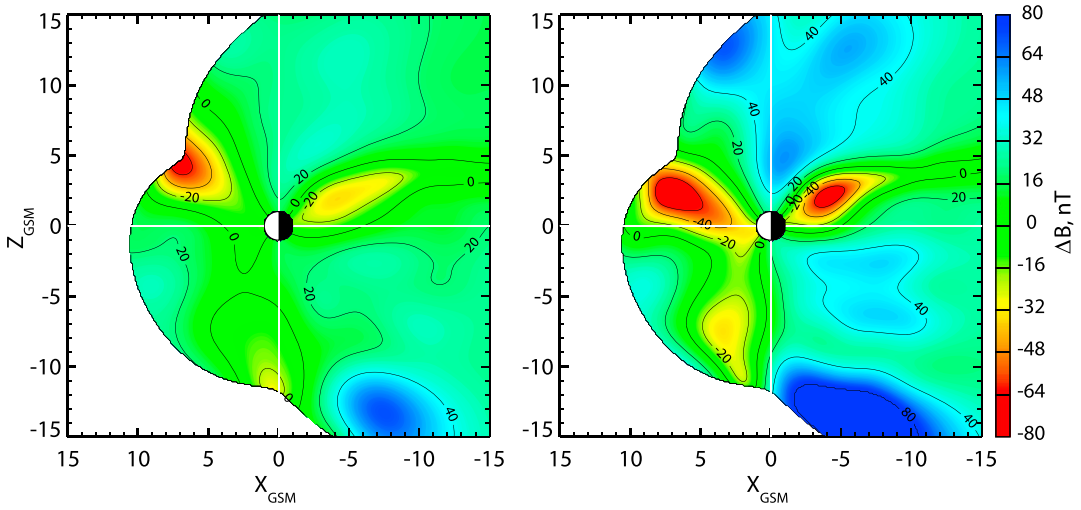

Figure 6. Meridional distributions of ΔB in the tilted magnetospheric configuration ($\psi = 30°$), for two extreme values of the N-index: (left) $N = 0$ and (right) $N = 2$. All other model parameters have the same values: $P_d = 2$ nPa and $SYM\text{-}H = 0$.

manifesting its larger "rigidity" under southward IMF conditions and, conversely, its being more "elastic" for northward IMF. Just that very effect was detected in an earlier data-based study of the tilt-related tail current deformation [*Tsyganenko and Fairfield*, 2004] and confirmed in our later work [*Tsyganenko et al.*, 2015]. A final comment should be made regarding the extended areas of unrealistically strong field compression in the outermost part of the southern tail lobe (dark blue areas in the bottom of both panels in Figure 6). This is an apparent effect of insufficient data coverage at high GSM latitudes during the solstice periods, inevitably resulting from the seasonal rotation of the spacecraft apogees in GSM/GSE coordinates. A possible remedy to that kind of problem can be to combine the RBF approach with the modular models, as discussed in more detail in the next section.

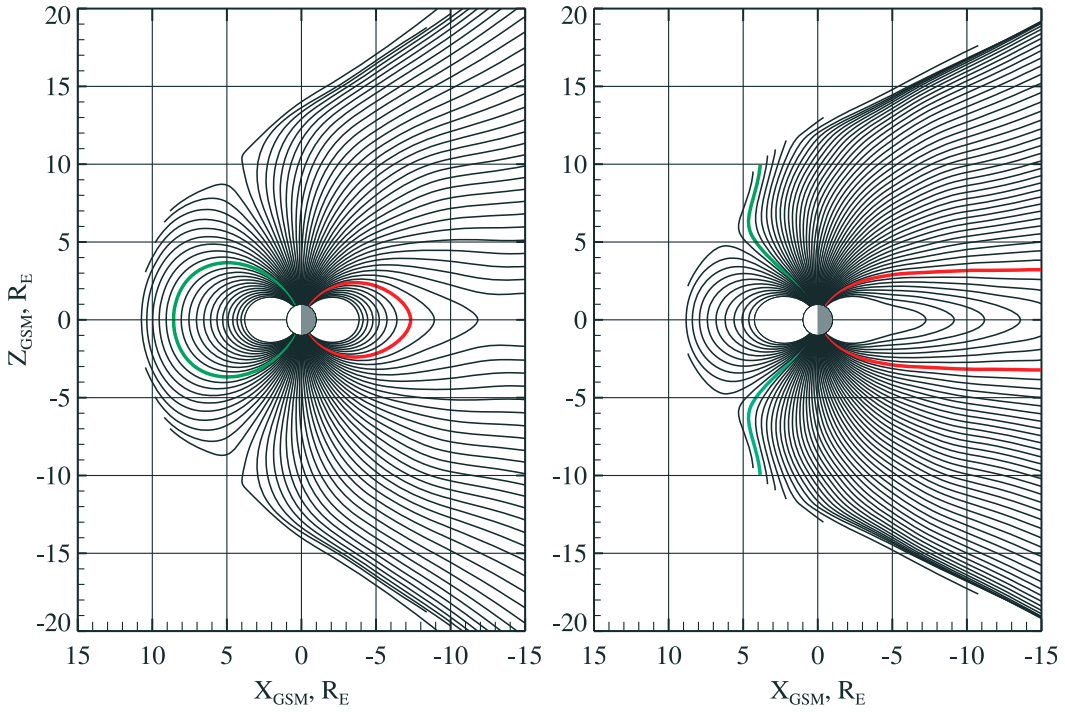

Figure 7. Two sample field line configurations corresponding to (left) quiet time and (right) storm time conditions. Field lines with foot point latitudes 66° at midnight and 71° at noon are highlighted by red and green colors, respectively. Note the dramatic difference between the plots in the field line stretch and in the dayside cusps position/mapping.

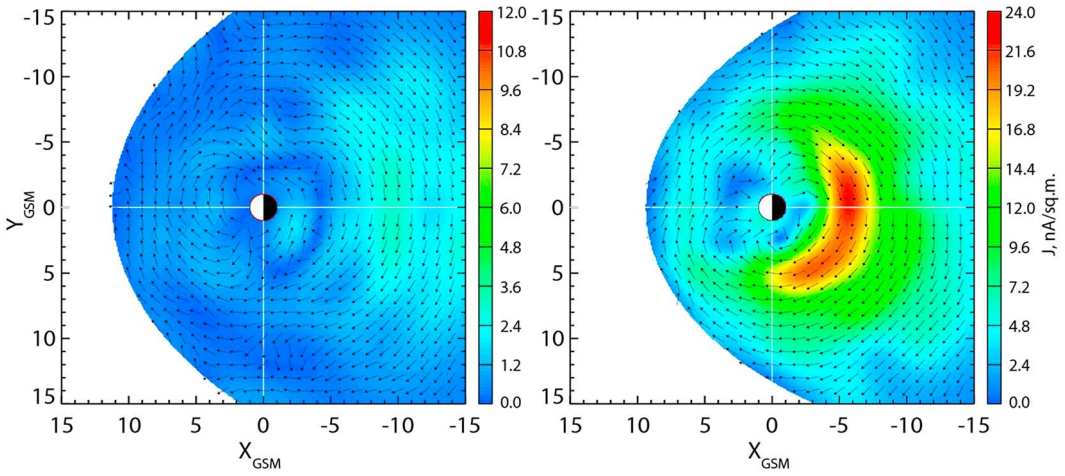

Figure 8. Equatorial distributions of the electric current volume density, calculated as the curl of the model **B** and corresponding to the same quiet and storm time sets of the model parameters as in Figures 5 and 7. Note the twofold difference in the color scaling range.

Figure 7 presents two sample field line configurations representing quiet ($P_d = 2$ nPa, $N = 0$, *SYM-H*=0, Figure 7, left) and storm time ($P_d = 4$ nPa, *SYM-H*=−150, $N = 2$, Figure 7, right) conditions, with the same values of the model parameters as those in Figure 5. To help visualize the dramatic difference in the field line stretch between these two cases, the lines with foot point latitudes of 66° and 71° are highlighted by red and green colors, respectively. Under the quietest conditions the magnetic field configuration is very close to a dipole-like inside $R \leq 10\,R_E$ but gets remarkably stretched immediately outward from that distance. By contrast, under disturbed conditions the inner magnetospheric field becomes much more stretched and depressed, and the magnetic flux gets swept from there to larger radial distances, which results in larger positive B_z at $10 \leq R \leq 20\,R_E$ and more pronounced field line connectivity across the equatorial plane. Whether or not the apparent neutral line at $X \sim -12\,R_E$ in Figure 7 (left) is real is hard to tell for two reasons: (1) the model field line plot inevitably represents an average of the mixture of individual transient configurations and (2) the RBF meshwork does not extend beyond $R \sim 15\,R_E$ and gets rather sparse in that outermost area, so that the accuracy of the model may be affected here by fringe effects. In this regard, it is also worth noting that both the present model and the old T89 [*Tsyganenko*, 1989] predict virtually the same degree of stretch under quiet conditions, with the 68° field line mapping to $R \approx 10 - 12\,R_E$.

One can also notice that the distant segments of the high-latitude tail lobe field lines have unrealistically straight shape and too large flaring angle. This is an artifact of lack of both data and of the RBF nodes at large distances, as clearly seen in Figure 2. The magnetic field in that area is a result of the outward linear extrapolation of **B** distribution beyond the model's validity region. In this regard, note that the present RBF model, by construction, has no explicit magnetopause as such. At any point of space, regardless of whether inside or outside the magnetopause, the model field is calculated by equations (1) and (2) with the coefficients $a_{i_{1,2}}$ being determined from only the intramagnetospheric data. As already said, the magnetic field in the vicinity of the magnetopause and outside is, in fact, a result of a smooth outward extrapolation of the model field beyond the region covered by measurements. The magnetopause appears in such a case as a "de facto" surface separating two families of field lines: those with at least one intersection with the Earth's surface and those with no connection to Earth at all. Such a de facto magnetopause is quite similar to that in the old T89 model, also constructed without an explicit boundary. In principle, one can envision a future RBF modeling study based on both magnetospheric and magnetosheath data (and, as an option, even those taken in the solar wind). Models of that kind would be able to reproduce the magnetopause layer in the form of more or less abrupt field jumps or reversals. However attractive such a project might appear, it would require much wider spacecraft data coverage and complete reprocessing of the existing database, which currently remains beyond our grasp.

Two plots in Figure 8 were obtained using the same sets of model parameters as in Figure 7 and display the corresponding equatorial distributions of the electric current volume density. Note (a) the dramatic earthward shift of the current peak, from ~10 R_E at quiet conditions to 5–6R_E for the storm time case, and (b) the strong

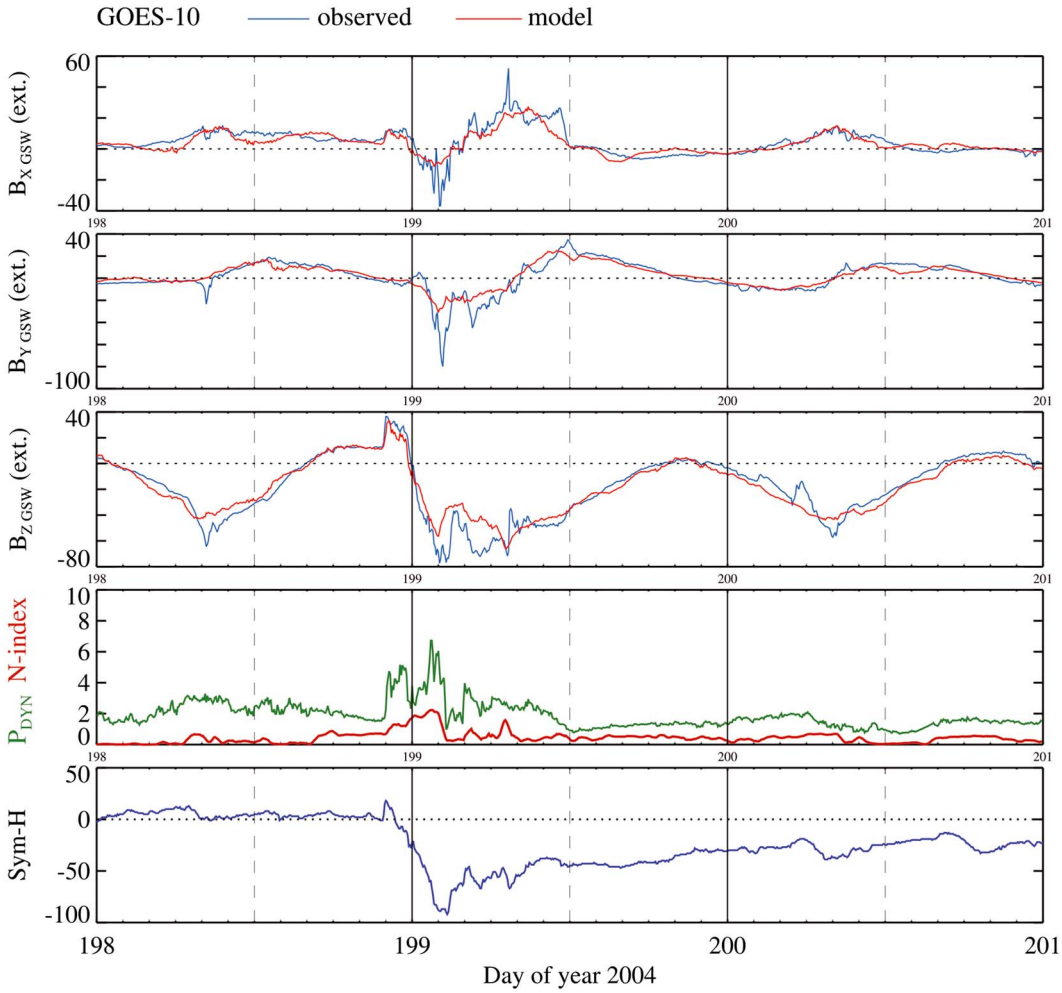

Figure 9. Comparing the RBF model output with GOES 10 magnetometer data taken during the storm of 16–17 July 2004. First to third panels compare the observed GSW components of the magnetic field (blue) with the model field (red). The plots correspond to only the external part of the field, with the Earth's contribution (IGRF) subtracted. The fourth panel shows the concurrent variation of the solar wind ram pressure (green) and the interplanetary *N*-index (red), and the fifth panel shows the concurrent variation of the *SYM-H* index.

dawn-dusk asymmetry of the ring current that develops in the disturbed configuration and corresponds to the asymmetry of ΔB depression in Figure 5 (bottom right). An interesting feature here is a well-developed inner eastward ring current in the quiet configuration and, on the other hand, its complete disappearance in the storm time diagram. An obvious physical reason is the pileup of freshly injected energetic particles in the innermost magnetosphere during storms. As a result, the peak of plasma pressure and, hence, the inner slope of the pressure profile with $dP/dr > 0$ (colocated with the eastward current) shift to lower altitudes with much higher magnetic field intensity which, in effect, completely suppresses the eastward current.

6. Discussion

The primary goal of this paper is to demonstrate, as a matter of principle, the possibility to build a full-scale model of the near magnetosphere based solely on data and without relying on any preconceived idea of the electric current distribution. Note, however, that while our approach lends maximum freedom to the geometrical structure of the magnetic field, the model is yet much less flexible in the parametric space, and there is still ample room for further exploration and improvement. In particular, the adopted form (10)–(13) of the RBF node magnitudes assumes from the outset the linear dependence on both the *SYM-H* and *N*-indices. While the *SYM-H* index more or less directly reflects the actual magnitude of the inner geospace currents at a given time moment, the *N*-index, by contrast, merely quantifies the current rate of the interplanetary

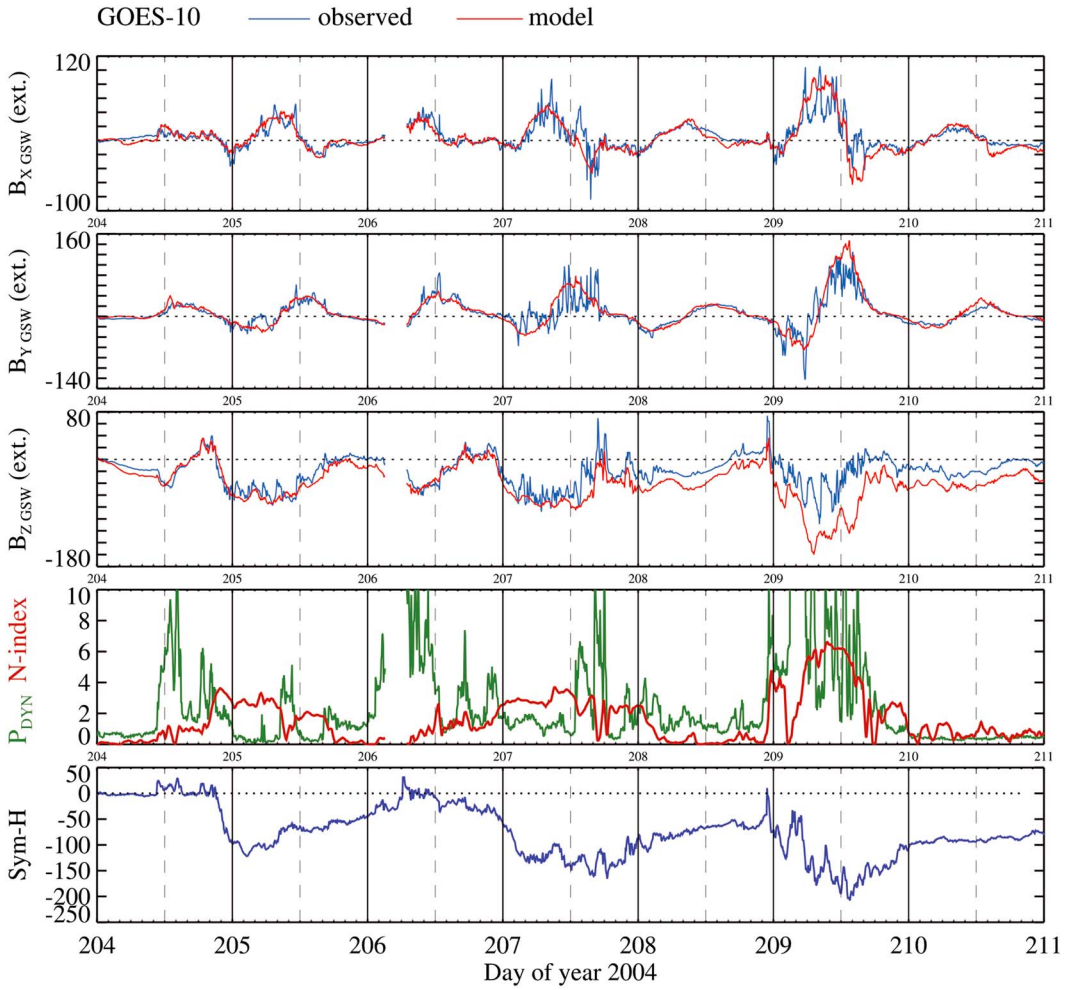

Figure 10. Same as in Figure 9 but for the triple storm of 22–28 July 2004. Note the growing overestimate in the model B_z in the second half of the interval.

magnetic flux intake into the magnetosphere. Its impact on the strength of the magnetospheric currents not only lags in time but is also essentially nonlinear, with saturation effects coming into play during strong disturbances [e.g., *Siscoe et al.*, 2004, and references therein]. Another limitation is the model's inability to accurately reproduce local/transient variations in the inner magnetotail region. This is an inevitable deficiency inherent to all statistical models, stemming from the temporal/spatial averaging of many largely diverse individual field configurations in the course of a substorm. Finally, the current version of the model does not differentiate between the cases of a long recovery phase after a strong storm and much shorter ones following disturbances of moderate and small intensity. In other words, the model yet lacks the ability to properly take into account the time history of an event.

To illustrate the above arguments, we show in Figures 9 and 10 two examples of validating the model against independent magnetometer data of geosynchronous satellites, not included in the modeling data set and taken during two storms of different intensity. Both figures have the same format with five panels, displaying three GSW components of the external part (i.e., with Earth's contribution subtracted) of the observed (blue) and model (red) field, the concurrent variation of the solar wind ram pressure and *N*-index (fourth panel from top, green and red traces, respectively), and the *SYM-H* index (fifth panel). Figure 9 corresponds to a moderate storm of 16–17 July 2004, as seen in the GOES 10 magnetogram. Overall, all three field components are reproduced fairly well by the model, including a sudden commencement pulse in B_z due to the initial gust of the solar wind at 22:00 UT of 16 July. At the same time, the model underestimates the field response during the storm main phase and almost completely smooths out the intense substorm-related spikes and oscillations.

Figure 10 presents a more complex case of a triple storm of 22–28 July 2004, with three increasingly deeper peaks of *SYM-H* on 23, 25, and 27 July. Note that the agreement between the observed and model B_z traces is fairly good during the first half of the interval (days 204-207) but becomes progressively worse starting from the main phase of the second storm. At the same time, one can notice that the *SYM-H* relaxation level during the three consecutive recovery phases has a clear trend to shift to lower and lower values. In our opinion, this is a key fact that explains the increasingly large overshoot in the model B_z depression toward the end of the whole interval. Namely, as a result of the recurring storms following at relatively short intervals, the newly injected energetic particles get pumped deeper and deeper into the innermost magnetosphere, and the ring current shrinks earthward to progressively lower L shells, well inside the synchronous orbit. As a consequence, the field depression deepens mainly in the immediate vicinity of Earth (reflected in lower *SYM-H* values), while at GOES orbit the effect is either weaker or even opposite to that at low altitudes. However, our model is "trained" mostly on weaker events, in which the ground and synchronous field depressions correlate much better. This results in progressively larger overestimates of the modeled nightside depression at GOES orbit, found in similar calculations for increasingly stronger storms (not reproduced for brevity reasons). The above example exposes once again the parameterization as a major remaining problem to be addressed in future studies.

Another focus area in the development of a global model is the issue of the data coverage. The seemingly dense and mostly gapless distributions of the data records shown in Figures 2 and 3 combine observations made in all seasons. However, because of the annual shift of spacecaft orbits, the coverage for selected intervals of the geodipole tilt may be not that good, which can result in model artifacts such as the areas of unrealistically compressed field in the distant southern tail lobe (Figure 6). As briefly noted in the end of section 5, that problem can potentially be solved in the framework of a "hybrid" approach, in which a module-based model, e.g., like TA15, is fitted first to the database, after which a flexible RBF model is used to further minimize the residual field. Besides offering a potential solution to the problem of data coverage at large distances, that approach may be of help to resolve a fine structure of the field at low altitudes. In particular, as was shown in AT16, the RBF model in its current realization cannot properly represent the field of Birkeland currents at ionospheric heights, because of both insufficient resolution of the node meshwork and lack of high-quality low-altitude data. A possible remedy could be to take advantage of the fact that in the range of distances between 1 and 3–4 R_E the field-aligned currents flow nearly along the dipolar field lines, where one can model their effect using the existing "modular" methods, e.g., those employed in TA15. At larger distances, the actual configuration of the field-aligned currents (FACs) is much less known, but their transverse scale is substantially larger there, which would allow the RBF component to effectively take over and to properly correct the first-guess FAC configuration in that region. It is our plan to explore in detail that attractive approach in a future study.

7. Summary

In this work we presented an empirical model of the magnetospheric magnetic field, based on the largest ever volume of space magnetometer data and using a minimum of preconceived notions/assumptions on the spatial structure of the associated electric currents. The paper is based on and further develops our previously published idea to combine the toroidal/poloidal representation of the magnetic field with expanding the corresponding generating potentials into sums of the radial basis functions. The model is parameterized by presenting the magnitude coefficients of the RBF field sources as first-order polynomials of the principal driving variables, including the square root of the solar wind pressure, the corrected *SYM-H* index, the interplanetary coupling index *N*, and the IMF B_y component. As a result, the model was found to provide the best ever merit parameters, in terms of the ratio of the RMS residual *Q* to the RMS observed field, as well as the highest ever correlations between the individual components of the observed and model field, especially for B_y. The model has been tested against independent data of the geosynchronous GOES 10 satellite and, in general, was found to faithfully reproduce all three components of the observed field. At the same time, the validation revealed systematic overestimates of the model field depression on the nightside during strong storms, most likely due to lack of information in the model parameters that would allow to clearly discriminate between the storm phases. The most promising area for future research is to combine the present RBF methodology with the traditional modular approach, which will help overcome problems related to insufficient data coverage in remote corners of the geometric and parametric space.

Acknowledgments
The data and source codes are available on request from the authors and will be made accessible from our Web page http://geo.phys.spbu.ru/~tsyganenko/modeling.html. It is a pleasure to acknowledge the teams and PIs of all experiments whose data contributed to this study. Geotail MGF data were provided by the PIs, S. Kokubun (STEL) and T. Nagai (Tokyo Institute of Technology, Japan). The data of Polar MGF experiment were made available online by the UCLA team led by the PI C.T. Russell. The Cluster magnetometer, spacecraft ephemeris, and CIS instrument data were obtained from the NSSDC CDAWEB online facility (originally provided by the PIs: A. Balogh, M. Tatrallyay, and H. Reme, respectively). NASA contract NAS5-02099 and V. Angelopoulos are acknowledged for use of THEMIS Mission data; specifically, K.H. Glassmeier, U. Auster, and W. Baumjohann are acknowledged for the use of FGM data provided under the lead of the Technical University of Braunschweig and with financial support through the German Ministry for Economy and Technology and the German Center for Aviation and Space (DLR) under contract 50 OC 0302. We acknowledge the NASA Van Allen Probes and C. Kletzing (University of Iowa) for use of the RBSP-A and RBSP-B EMFISIS data. GOES 10 magnetometer data were obtained from the CDAWEB resource (originally provided by H. Singer, NOAA). High-Resolution OMNI interplanetary data were obtained from the SPDF OMNIWEB interface (R. McGuire and N. Papitashvili). This work was supported by the Russian Science Foundation grant 14-17-00072.

References

Andreeva, V. A., and N. A. Tsyganenko (2016), Reconstructing the magnetosphere from data using radial basis functions, *J. Geophys. Res. Space Physics*, *121*, 2249–2263, doi:10.1002/2015JA022242.

Boynton, R. J., M. A. Balikhin, S. A. Billings, H. L. Wei, and N. Ganushkina (2011), Using the NARMAX OLS-ERR algorithm to obtain the most influential coupling functions that affect the evolution of the magnetosphere, *J. Geophys. Res.*, *116*, A05218, doi:10.1029/2010JA015505.

Buhmann, M. (2003), *Radial Basis Functions: Theory and Implementations*, Cambridge Univ. Press, Cambridge, U. K.

Elsasser, W. M. (1946), Induction effects in terrestrial magnetism Part I. Theory, *Phys. Rev.*, *69*(3–4), 106–116, doi:10.1103/PhysRev.69.106.

Gershenfeld, N. (2003), *The Nature of Mathematical Modeling*, Cambridge Univ. Press, Cambridge, U. K.

Hones, E. W., R. D. Zwickl, T. A. Fritz, and S. J. Bame (1986), Structural and dynamical aspects of the distant magnetotail determined from ISEE-3 plasma measurements, *Planet. Space Sci.*, *34*, 889–901.

Kaymaz, Z., G. L. Siscoe, J. G. Luhmann, R. P. Lepping, and C. T. Russell (1994), Interplanetary magnetic field control of magnetotail magnetic field geometry: IMP 8 observations, *J. Geophys. Res.*, *104*, 11,113–11,126.

Kurihara, Y. (1965), Numerical integration of the primitive equations on a spherical grid, *Mon. Weather Rev.*, *93*(7), 399–415.

Lin, R. L., X. X. Zhang, S. Q. Liu, Y. L. Wang, and J. C. Gong (2010), A three-dimensional asymmetric magnetopause model, *J. Geophys. Res.*, *115*, A04207, doi:10.1029/2009JA014235.

Lui, A. T. Y. (1986), Solar wind influence on magnetotail configuration and dynamics, in *Solar Wind-Magnetosphere Coupling*, edited by Y. Kamide and J. A. Slavin, pp. 671–690, Kluwer, Norwell, Mass.

Newell, P. T., T. Sotirelis, K. Liou, C.-I. Meng, and F. J. Rich (2007), A nearly universal solar wind-magnetosphere coupling function inferred from 10 magnetospheric state variables, *J. Geophys. Res.*, *112*, A01206, doi:10.1029/2006JA012015.

Press, W. H., S. A. Teukolsky, W. T. Vetterling, and B. P. Flannery (1992), *Numerical Recipes*, 2nd ed., Cambridge Univ. Press, New York.

Sergeev, V. A. (1987), On the penetration of IMF B_y into the geomagnetic tail, *Geomagn. Aeron., Engl. Transl.*, *27*, 612–614.

Siscoe, G., J. Raeder, and A. J. Ridley (2004), Transpolar potential saturation models compared, *J. Geophys. Res.*, *109*, A09203, doi:10.1029/2003JA010318.

Sitnov, M. I., N. A. Tsyganenko, A. Y. Ukhorskiy, and P. C. Brandt (2008), Dynamical data-based modeling of the stormtime geomagnetic field with enhanced spatial resolution, *J. Geophys. Res.*, *113*, A07218, doi:10.1029/2007JA013003.

Sitnov, M. I., N. A. Tsyganenko, A. Y. Ukhorskiy, B. J. Anderson, H. Korth, A. T. Y. Lui, and P. C. Brandt (2010), Empirical modeling of a CIR-driven magnetic storm, *J. Geophys. Res.*, *115*, A07231, doi:10.1029/2009JA015169.

Stephens, G. K., M. I. Sitnov, J. Kissinger, N. A. Tsyganenko, R. L. McPherron, H. Korth, and B. J. Anderson (2013), Empirical reconstruction of storm time steady magnetospheric convection events, *J. Geophys. Res. Space Physics*, *118*, 6434–6456, doi:10.1002/jgra.50592.

Stephens, G. K., M. I. Sitnov, A. Y. Ukhorskiy, E. C. Roelof, N. A. Tsyganenko, and G. Le (2016), Empirical modeling of the storm time innermost magnetosphere using Van Allen Probes and THEMIS data: Eastward and banana currents, *J. Geophys. Res. Space Physics*, *121*, 157–170, doi:10.1002/2015JA021700.

Stern, D. P. (1976), Representation of magnetic fields in space, *Rev. Geophys. Space Phys.*, *14*, 199–214.

Troshichev, O., and A. Janzhura (2012), *Space Weather Monitoring by Ground-Based Means: PC Index*, Springer, Berlin.

Tsyganenko, N. A. (1989), A magnetospheric magnetic field model with a warped tail current sheet, *Planet. Space Sci.*, *37*, 5–20.

Tsyganenko, N. A. (1996), Effects of the solar wind conditions on the global magnetospheric configuration as deduced from data-based field models, in *European Space Agency Publication ESA SP-389*, pp. 181–185.

Tsyganenko, N. A. (2002a), A model of the near magnetosphere with a dawn-dusk asymmetry: 1. Mathematical structure, *J. Geophys. Res.*, *107*(A8), 1179, doi:10.1029/2001JA000219.

Tsyganenko, N. A. (2002b), A model of the near magnetosphere with a dawn-dusk asymmetry: 2. Parametrization and fitting to observations, *J. Geophys. Res.*, *107*(A8), 1176, doi:10.1029/2001JA000220.

Tsyganenko, N. A. (2009), Magnetic field and electric currents in the vicinity of polar cusps as inferred from Polar and Cluster data, *Ann. Geophys.*, *27*, 1573–1582, doi:10.5194/angeo-27-1573-2009.

Tsyganenko, N. A. (2013), Data-based modelling of the Earth's dynamic magnetosphere: A review, *Ann. Geophys.*, *31*, 1745–1772, doi:10.5194/angeo-31-1745-2013.

Tsyganenko, N. A., and V. A. Andreeva (2014), On the "bowl-shaped" deformation of planetary equatorial current sheets, *Geophys. Res. Lett.*, *41*, 1079–1084, doi:10.1002/2014GL059295.

Tsyganenko, N. A., and V. A. Andreeva (2015), A forecasting model of the magnetosphere driven by an optimal solar wind coupling function, *J. Geophys. Res. Space Physics*, *120*, 8401–8425, doi:10.1002/2015JA021641.

Tsyganenko, N. A., and D. H. Fairfield (2004), Global shape of the magnetotail current sheet as derived from Geotail and Polar data, *J. Geophys. Res.*, *109*, A03218, doi:10.1029/2003JA010062.

Tsyganenko, N. A., and M. I. Sitnov (2005), Modeling the dynamics of the inner magnetosphere during strong geomagnetic storms, *J. Geophys. Res.*, *110*, A03208, doi:10.1029/2004JA010798.

Tsyganenko, N. A., and M. I. Sitnov (2007), Magnetospheric configurations from a high-resolution data-based magnetic field model, *J. Geophys. Res.*, *112*, A06225, doi:10.1029/2007JA012260.

Tsyganenko, N. A., S. B. P. Karlsson, S. Kokubun, T. Yamamoto, A. J. Lazarus, K. W. Ogilvie, C. T. Russell, and J. A. Slavin (1998), Global configuration of the magnetotail current sheet as derived from Geotail, Wind, IMP 8 and ISEE 1/2 data, *J. Geophys. Res.*, *103*, 6827–6841.

Tsyganenko, N. A., V. A. Andreeva, and E. I. Gordeev (2015), Internally and externally induced deformations of the magnetospheric equatorial current as inferred from spacecraft data, *Ann. Geophys.*, *33*, 1–11, doi:10.5194/angeo-33-1-2015.

Wolf-Gladrow, D. A. (1987), *An Introduction to Poloidal and Toroidal Fields*, p. 54, Mitt, Inst. Geophys. Meteorol. Univ. Koln, Koeln.